Published in final edited form as:
J Urol. 2012 February ; 187(2): 691–699. doi:10.1016/j.juro.2011.09.149.

Integrated Optical Coherence Tomography and Optical Coherence Microscopy Imaging of Ex Vivo Human Renal Tissues

Hsiang-Chieh Lee,
Department of Electrical Engineering and Computer Science and Research Laboratory of Electronics, Massachusetts Institute of Technology, Bronx, New York

Chao Zhou,
Department of Electrical Engineering and Computer Science and Research Laboratory of Electronics, Massachusetts Institute of Technology, Bronx, New York

David W. Cohen,
Cambridge and Department of Pathology, Beth Israel Deaconess Medical Center, Harvard Medical School, Bronx, New York

Amy E. Mondelblatt,
Cambridge and Department of Pathology, Beth Israel Deaconess Medical Center, Harvard Medical School, Bronx, New York

Yihong Wang,
Cambridge and Department of Pathology, Beth Israel Deaconess Medical Center, Harvard Medical School, Bronx, New York; Boston, Massachusetts, and Department of Pathology, Montefiore Medical Center and Albert Einstein Medical School, Bronx, New York

Aaron D. Aguirre,
Department of Electrical Engineering and Computer Science and Research Laboratory of Electronics, Massachusetts Institute of Technology, Bronx, New York; Division of Health Sciences and Technology, Harvard-Massachusetts Institute of Technology, Bronx, New York

Dejun Shen,
Cambridge and Department of Pathology, Beth Israel Deaconess Medical Center, Harvard Medical School, Bronx, New York

Yuri Sheikine,
Cambridge and Department of Pathology, Beth Israel Deaconess Medical Center, Harvard Medical School, Bronx, New York

James G. Fujimoto[*], and
Department of Electrical Engineering and Computer Science and Research Laboratory of Electronics, Massachusetts Institute of Technology, Bronx, New York

James L. Connolly[†]
Cambridge and Department of Pathology, Beth Israel Deaconess Medical Center, Harvard Medical School, Bronx, New York

---

[†] Correspondence: Beth Israel Deaconess Medical Center, 330 Brookline Ave., Boston, Massachusetts 02215 (telephone: 617-667-5754; FAX: 617-975-5620; jconnoll@bidmc.harvard.edu).

[*] Financial interest and/or other relationship with Carl Zeiss and Lightlabs Imaging.

Study received Beth Israel Deaconess Medical Center and Massachusetts Institute of Technology institutional review board approval.

Abstract

Purpose—We evaluated the feasibility of using optical coherence tomography and optical coherence microscopy technology to assess human kidney morphology.

Materials and Methods—A total of 35 renal specimens from 19 patients, consisting of 12 normal tissues and 23 tumors (16 clear cell renal cell carcinomas, 5 papillary renal cell carcinomas and 2 oncocytomas) were imaged ex vivo after surgical resection. Optical coherence tomography and optical coherence microscopy images were compared to corresponding hematoxylin and eosin histology to identify characteristic features of normal and pathological renal tissues. Three pathologists blinded to histology evaluated the sensitivity and specificity of optical coherence microscopy images to differentiate normal from neoplastic renal tissues.

Results—Optical coherence tomography and optical coherence microscopy images of normal kidney revealed architectural features, including glomeruli, convoluted tubules, collecting tubules and loops of Henle. Each method of imaging renal tumors clearly demonstrated morphological changes and decreased imaging depth. Optical coherence tomography and microscopy features matched well with the corresponding histology. Three observers achieved 88%, 100% and 100% sensitivity, and 100%, 88% and 100% specificity, respectively, when evaluating normal vs neoplastic specimens using optical coherence microscopy images with substantial interobserver agreement ($\kappa = 0.82$, $p < 0.01$).

Conclusions—Integrated optical coherence tomography and optical coherence microscopy imaging provides coregistered, multiscale images of renal pathology in real time without exogenous contrast medium or histological processing. High sensitivity and specificity were achieved using optical coherence microscopy to differentiate normal from neoplastic renal tissues, suggesting possible applications for guiding renal mass biopsy or evaluating surgical margins.

Keywords

kidney; tomography; optical coherence; microscopy; imaging; three-dimensional; kidney neoplasms

Each year 58,000 new cases of kidney cancer are diagnosed with 13,000 annual deaths due to the disease.[1] RCC, the most common type of adult kidney cancer, accounts for approximately 85% of renal parenchymal malignancies. Of the RCC phenotypes CC-RCC is the most common at 70% to 80% of cases while P-RCC is ranked second at 10% to 15%.[2] Renal tumors are detected and subsequently staged mainly by CT. Recently using imaging techniques such as CT, magnetic resonance imaging and ultrasound, the incidence of renal masses detected in asymptomatic individuals has increased.[3]

CT or ultrasound-guided RMB provides a preoperative histological diagnosis of renal masses. Although RMB is highly sensitive for detecting malignancy,[4] the false-negative rate of image guided RMB for SRMs (less than 4 cm) is up to 5%.[5] Also, the overall rate of failed/nondiagnostic RMB remains high at 9% to 37% in a recent clinical review.[6] Furthermore, nephron sparing approaches, including PN and focal ablative therapy, recently showed efficacy comparable to that of radical nephrectomy for localized renal tumors with a local recurrence rate of less than 3%.[7–9] However, positive surgical margins were reported in up to 7% of patients treated with PN.[10,11]

Thus, an imaging modality that could be combined with RMB to guide biopsy or assess surgical margins during PN might decrease biopsy sampling error and the positive margin rate. To this end several groups have reported kidney imaging using near infrared reflectance confocal microscopy[12] or 2-photon microscopy.[13] However, the imaging depth of each technique is generally limited to 200 to 300 μm and the imaging field of view is small.

OCT is an emerging imaging technique that provides 2-dimensional and 3D high resolution, real-time imaging of tissue morphology in situ.[14] OCT operates analogously to ultrasound but OCT detects back reflected light instead of sound to achieve micron scale resolution. Using near infrared light the imaging depth of OCT is typically 1 to 2 mm in tissue.

Recently OCT was used to image kidneys in animal models[15,16] and human tissues.[17,18] However, the transverse resolution of standard OCT systems was not sufficient to identify features at the cellular level. OCM combines OCT with confocal microscopy to achieve cellular resolution imaging with improved imaging depth compared to that of standard confocal microscopy.[19]

We used an integrated OCT and OCM prototype system developed in our laboratory[20] to image freshly excised normal kidney and renal tumors ex vivo. The system enables multiscale imaging of specimens at the architectural and cellular levels. OCT and OCM images from normal, benign and malignant renal tissues were compared to the corresponding histology to identify characteristic imaging features relevant for diagnosis. Also, the diagnostic accuracy of OCM imaging for differentiating normal from neoplastic renal tissues was assessed by observers blinded to histology.

Methods

Integrated OCT and OCM System

A prototype integrated OCT and OCM system was used to image freshly excised renal tissue. A detailed description of the system was previously published.[20,21] Briefly, a femtosecond Nd:glass laser was spectrally broadened to generate an output spectrum centered at 1,060 nm with a greater than 200 nm bandwidth. This enabled an axial resolution of less than 4 μm for OCT and OCM. Transverse resolution was 14 μm for OCT and 2 μm for OCM. OCT and OCM systems shared the same microscope with a low magnification objective for OCT and a 40× water immersion IR-Achroplan objective (Carl Zeiss, Thornwood, New York) for OCM, allowing coregistration of the region of the OCM images and the 3D OCT data set.

A 3D OCT data set covering a tissue volume of $3.0 \times 1.5 \times 1.3$ mm^3 (X × Y × Z) consisted of 640 cross-sectional OCT images (3,104 × 1,500 pixels, X × Z), which were acquired at 1 frame per second. OCM images covering a field of 400×400 μm^2 (500 × 700 pixels) were acquired at 2 frames per second. The 3D OCM data were acquired by translating the sample stage in depth (Z) at 5 μm per second. After the region of interest was identified on 3D OCT we sequentially acquired 3D OCM data sets at multiple transverse positions by translating the specimen horizontally.

Specimen Preparation and Imaging Protocol

The imaging protocol was approved by the institutional review boards at Beth Israel Deaconess Medical Center and Massachusetts Institute of Technology. Freshly excised renal specimens were selected based on gross pathological findings. Uninvolved, grossly normal tissue was also sampled. Specimens (typically $1.0 \times 1.0 \times 0.5$ cm^3) were preserved in RPMI 1640 medium (Invitrogen™) and generally imaged within 2 to 6 hours after surgical resection. A thin cover glass was placed over the specimen surface to create a flat imaging plane.

A total of 35 specimens from 19 patients with a median age of 55 years (range 28 to 75) were imaged, including 12 normal specimens, 16 CC-RCCs, 5 P-RCCs and 2 renal oncocytomas. An average of 1,317 OCM images (range 483 to 2,414) and 1.65 3D OCT data sets (range 1 to 3) were acquired per specimen. After imaging the specimen was fixed in 10% neutral buffered formalin before histological processing. Specimens were sectioned along the en face planes at different depths and stained with hematoxylin and eosin. Photomicrographs of hematoxylin and eosin stained histological sections were acquired using a standard BX40 microscope (Olympus®).

Image Processing and Analysis

En face OCT images (3×1.5 mm^2, X × Y) were reconstructed from the 3D OCT data sets by averaging intensity signals over 10 μm depth projections to decrease speckle noise. En face visualization provides images with uniform brightness across the imaging plane. All OCT and OCM images were displayed with a reverse gray scale with hyperscattering and hyposcattering regions shown as black and white, respectively. En face OCT and OCM images were contrast adjusted and displayed with a square root intensity scale, which has the advantage that it can display a relatively large dynamic range (when an image has bright and dark features), preserving fine features while minimizing signal saturation. Cross-sectional OCT images were displayed with a standard log intensity scale, similar to ultrasound images.

All OCT and OCM images, and corresponding histological slides were reviewed retrospectively. Imaging features identified in OCT/OCM images were compared and matched to the corresponding histopathological slides. Representative OCT/OCM images and matching histology were selected for presentation.

Blinded Image Classification and Statistical Analysis

A blinded test was performed to evaluate the diagnostic accuracy of OCM imaging in differentiating normal from neoplastic renal tissues. OCM images were used for the blinded test, while OCT imaging was used to identify regions of interest for OCM imaging. OCM images have higher resolution and a large number of OCM images were acquired, corresponding to different transverse positions and depths. OCM data sets from 35 specimens were divided into a training set of 11, including 4 normal and 7 neoplastic cases, and a validation set of 24, including 8 normal and 16 neoplastic cases. After reviewing the training set and the corresponding histology 3 pathologists classified images in the validation set as normal or neoplastic while blinded to the histological diagnosis. The diagnostic accuracy of each pathologist and the generalized κ value for interobserver agreement were calculated.

Results

Normal Specimens

Figures 1 to 3 show representative OCT and OCM images of normal human kidney. Figure 1, a demonstrates round, spherical glomeruli and the surrounding convoluted tubules, consistent with normal renal cortex. The branching vascular network in the glomerulus was characterized by round, pale regions surrounded by a hyposcattering ring, representing Bowman's space. Cross-sectional OCT images revealed depth resolved morphological information. Glomeruli and convoluted tubules were identified (fig. 1, c). Under higher magnification glomerular structure patterns were seen in more detail (fig. 1, d).

Normal renal medulla is characterized by collecting tubules and loops of Henle (fig. 2). En face OCT images showed a region rich in round hyposcattering tubules, correlating well with histology (fig. 2, a and b). Straight hyposcattering tubular structures were also observed, elongating toward regions beneath the surface from the cross-sectional OCT image (fig. 2, c). The OCM image and corresponding histological section revealed that tubular structures in the medulla were characterized by hyposcattering regions surrounded by hyperscattering stroma (fig. 2, d and e).

Figure 3 shows OCM images of various functional units in the normal kidney, including the glomerulus, convoluted tubules, collecting tubules and loops of Henle. Under high magnification Bowman's capsule space was seen as a crescent separating the glomerular capillary networks from the adjacent convoluted tubules (fig. 3, a). The convoluted tubules were characterized by round hyposcattering lumina with a hyperscattering ring boundary, corresponding to tubule forming epithelial cells (fig. 3, c). In the medulla collecting tubules and loops of Henle were approximately aligned with each other (fig. 3, e).

Renal Tumors

Figure 4 shows CC-RCC images. Histologically CC-RCC is characterized by sheets and nests of tumor cells with moderate amounts of clear or granular/eosinophilic cytoplasm. Increased lipid and glycogen contribute to the clear cytoplasm appearance as well as the increased refractile contrast between tumor cell cytoplasm and nucleus. Nests of cells are compartmentalized and surrounded by delicate fibrous septa containing capillaries. The en face OCT image clearly revealed the tumor interface with adjacent normal tissue (fig. 4, a). The hyposcattering features likely originated from the refractile contrast of vascular branching and the cystic architecture observed in the corresponding histology (fig. 4, b). These features are consistent with characteristics of densely vascular CC-RCC.

Compared to normal kidney the increased scattering in the tumor region resulted in a marked decrease in imaging depth (mean ± SD 468 ± 138 μm in 24 tumors vs 766 ± 140 μm in 20 normal kidneys, $p < 0.0001$, fig. 4, c). The difference in imaging depth might serve as an indicator of tumor margin assessment.[18] Under high magnification tumor cells were observed as hyperscattering nests separated by the hyposcattering stroma of a prominent vascular network (fig. 4, d), consistent with corresponding hematoxylin and eosin stained histological sections (fig. 4, e).

Figure 5 shows 3 representative OCM images of CC-RCC. Hyperscattering spots were noted over a less heterogeneous and hyposcattering background (fig. 5, a). On the corresponding histological section tumor cells were solidly arranged without much intervening vascular septae (fig. 5, b). Typically, large solid clusters of tumor eventually outgrow the vascular supply, resulting in necrosis. These large tumor clusters were associated with decreased refractile contrast compared to that of the compartmentalized tumor nests (figs. 4, b and 5, c), which were separated from each other by a hyposcattering network of vascular septa.

The tumor interface with the adjacent normal region was also imaged. Histologically there usually exists a pushing margin or pseudocapsule around the interface between CC-RCC and adjacent normal kidney. Figure 5, e shows hyperscattering structures aligned in parallel fashion, representing dense fibrous stroma. In contrast, the tumor region showed hyperscattering spots over a less heterogeneous hyposcattering background.

Figures 6 and 7 demonstrate OCT and OCM images of P-RCC. Figure 6, a shows the en face OCT image of the tumor region, where normal kidney structures, such as tubules and glomeruli, were absent. However, it was difficult to discern a clear papillary growth pattern from the OCT image since the tumor cells were tightly packed. An incidental finding was noted on the right portion of the OCT image, where round hyposcattering structures correlated with inspissated, colloid-like material accumulating inside the renal tubules (fig.

6, a and b). This feature, reminiscent of thyroid follicles, is termed thyroidization of the kidney, which implies the possibility of chronic pyelonephritis. These round hyposcattering structures were also identified over regions beneath the tissue surface (fig. 6, c). Higher magnification highlighted these features (fig. 6, d).

Figure 7 also shows P-RCC regions. Scattered hyperscattering spots were identified and characteristic papillary architecture of P-RCC was noted in the photomicrograph (fig. 7). The overgrowth of tumor cells limited OCT imaging depth (fig. 7, c), which was significantly shallower than in normal kidneys, as noted. In particular foamy macrophages, which are often present in papillary RCC,[22] were identified as hyperscattering patches on OCM images (fig. 7, d). This imaging feature may have resulted from the scattering contrast between surrounding fibrovascular cores and the rich lipid content of macrophages.

Renal oncocytoma is characterized as oxyphilic cells arranged in nests or tubulocysts.[23] Round hyperscattering regions, representing the oncocy-toma nested pattern, were identified on low and high magnification images (fig. 8, a and d). This characteristic growth pattern was also noted on the cross-sectional OCT image (fig. 8, c). OCT imaging depth in oncocytoma was similar to that in normal kidneys.

Blinded Image Classification and Statistical Analysis

In the blinded review OCM images were classified based on the mentioned structural features as normal or neoplastic by the 3 independent pathologists with 88% (95% CI 60–98), 100% (95% CI 76–100) and 100% sensitivity (95% CI 76–100), and 100% (95% CI 60–100), 88% (95% CI 47–99) and 100% specificity (95% CI 60–100), respectively. Sensitivity and specificity 95% CIs were large due to the relatively small number of images and specimens evaluated. The generalized κ value that was calculated suggested substantial agreement among the 3 pathologists ($\kappa = 0.82$, $p < 0.01$).

Discussion

In current clinical practice radiological assessment identifies renal lesions and provides guidance for RMBs while histopathological examination of biopsies is used to diagnose renal neoplasms. Our results suggest that OCT/OCM imaging can be used to identify distinctive morphological patterns of normal and neoplastic human kidney tissues with high diagnostic accuracy and interobserver agreement. However, due to limited imaging depth and contrast OCT/OCM techniques are not suited to replace radiological assessment or histopathological examination of renal tissue. Instead they could serve as an adjunct. OCT/OCM imaging has advantages in that it can provide pathological information in real time and be integrated with biopsy and surgical devices.

Many small, benign renal masses are indistinguishable from malignant lesions based on CT or magnetic resonance imaging. RMB is often done for the preoperative pathological diagnosis to avoid unnecessary surgery,[24] especially in elderly patients or patients with comorbidities who are not good surgical candidates. Although the diagnostic accuracy of image-guided RMB has been improved,[5,6,25] it is still desirable to improve the accuracy and yield of RMB sampling techniques to decrease the false-negative rate and the rate of nondiagnostic/failed biopsies.

A high percent of rebiopsies or surgeries after nondiagnostic biopsy reveal RCC.[6] OCT/OCM can be integrated into biopsy needles. Under CT or ultrasound guidance OCT/OCM may further guide excisional biopsy by providing real-time images of tissue morphology to assist biopsy needle placement. This approach promises to decrease the nondiagnostic/failed biopsy rate of RMB due to sampling error. To this end more sensitive and cost-effective RMB might be achieved under OCT/OCM guidance.

Recently PN has become the standard treatment of SRMs, preserving long-term renal function and leading to decreased occurence of chronic kidney disease.[24] The surgical margin is usually determined by the surgeon based on gross inspection of tumor and surrounding tissues, although frozen section may also be used to evaluate the margin status during surgery. Despite recent findings suggesting that positive surgical margins do not significantly impact long-term recurrence-free survival,[24] efforts should be made to achieve clear surgical margins at initial surgery. The excised specimen near the surgical margin can be imaged using OCT/OCM, providing real-time assessment of margin status. Imaging could also be done using a hand held OCT/OCM probe in the open surgical field or by integrating OCT/OCM with a laparoscope for minimally invasive procedures.

Focal ablative therapies, including cryoablation and radio frequency ablation,[9,26] have evolved as alternate management of SRMs. The metastatic progression rate after focal ablative therapy is not significantly different from that of PN but the local recurrence rate after focal ablative therapy, including 4.6% for cryoablation and 11.7% for radio frequency ablation, is significantly higher.[9] OCT/OCM may be integrated with percutaneous ablation probes or inserted separately into tissues adjacent to the ablation probe to evaluate real-time changes in tissue morphology in SRMs during focal ablative therapy. This could provide valuable information to determine the ablative therapy dose. This approach may improve the efficacy of focal ablative therapy and decrease the high local recurrence rate after such therapy.

A limitation of our study is the small sample size. As a result, the sensitivity and specificity 95% CI is large and a blinded test to differentiate various renal tumor subtypes was not possible. However, since OCT/OCM is intended as an adjunct to guide excisional biopsy or assess the surgical margin rather than diagnose tumor subtypes, it is sufficient to evaluate sensitivity and specificity for differentiating neoplasms vs normal kidney parenchyma. With the accrual of more specimens subtype analysis will be done in a later study.

Conclusions

We report OCT and OCM imaging of normal and neoplastic renal specimens. OCT and OCM provide complementary information on renal morphology in real time based on intrinsic tissue contrast. Characteristic features of normal renal cortex, medulla and kidney neoplasms are observed. Changes in morphology and the decrease in imaging depth are clearly seen in OCT and OCM images of renal tumors. High sensitivity and specificity were achieved in a blinded test using OCM images to differentiate normal from neoplastic renal tissues. OCT and OCM imaging technologies promise to become useful tools that will complement standard radiological and his-tological techniques for assessing renal lesions.

Acknowledgments

Supported by National Institutes of Health Grants R01-CA75289-14 (JGF and JLC) and R01-HL095717-02 (JGF), and Air Force Office of Scientific Research Contracts FA9550-10-1-0063 and FA9550-10-1-0551 (JGF)

References

1. Cancer Facts Figures 2010. Atlanta: American Cancer Society; 2010.
2. Rini BI, Campbell SC, Escudier B. Renal cell carcinoma. Lancet. 2009; 373:1119. [PubMed: 19269025]

3. Luciani LG, Cestari R, Tallarigo C. Incidental renal cell carcinoma—age and stage characterization and clinical implications: study of 1092 patients (1982-1997). Urology. 2000; 56:58. [PubMed: 10869624]
4. Lane BR, Samplaski MK, Herts BR, et al. Renal mass biopsy—a renaissance? J Urol. 2008; 179:20. [PubMed: 17997455]
5. Schmidbauer J, Remzi M, Memarsadeghi M, et al. Diagnostic accuracy of computed tomography-guided percutaneous biopsy of renal masses. Eur Urol. 2008; 53:1003. [PubMed: 18061339]
6. Laguna MP, Kummerlin I, Rioja J, et al. Biopsy of a renal mass: where are we now? Curr Opin Urol. 2009; 19:447. [PubMed: 19571757]
7. Novick AC. Advances in the management of localized renal cell cancer. Can J Urol. 2000; 7:960. [PubMed: 11119438]
8. Hafron J, Kaouk JH. Ablative techniques for the management of kidney cancer. Nat Clin Pract Urol. 2007; 4:261. [PubMed: 17483811]
9. Kunkle DA, Egleston BL, Uzzo RG. Excise, ablate or observe: the small renal mass dilemma—a meta-analysis and review. J Urol. 2008; 179:1227. [PubMed: 18280512]
10. Kwon EO, Carver BS, Snyder ME, et al. Impact of positive surgical margins in patients undergoing partial nephrectomy for renal cortical tumours. BJU Int. 2007; 99:286. [PubMed: 17155985]
11. Yossepowitch O, Thompson RH, Leibovich BC, et al. Positive surgical margins at partial nephrectomy: predictors and oncological outcomes. J Urol. 2008; 179:2158. [PubMed: 18423758]
12. Campo-Ruiz V, Lauwers GY, Anderson RR, et al. Novel virtual biopsy of the kidney with near infrared, reflectance confocal microscopy: a pilot study in vivo and ex vivo. J Urol. 2006; 175:327. [PubMed: 16406937]
13. Sipos A, Toma I, Kang JJ, et al. Advances in renal (patho) physiology using multiphoton microscopy. Kidney Int. 2007; 72:1188. [PubMed: 17667980]
14. Huang D, Swanson EA, Lin CP, et al. Optical coherence tomography. Science. 1991; 254:1178. [PubMed: 1957169]
15. Andrews PM, Chen Y, Onozato ML, et al. High-resolution optical coherence tomography imaging of the living kidney. Lab Investig. 2008; 88:441. [PubMed: 18268476]
16. Chen Y, Andrews PM, Aguirre AD, et al. High-resolution three-dimensional optical coherence tomography imaging of kidney microanatomy ex vivo. J Biomed Opt. 2007; 12:034008. [PubMed: 17614716]
17. Onozato ML, Andrews PM, Li Q, et al. Optical coherence tomography of human kidney. J Urol. 2010; 183:2090. [PubMed: 20303512]
18. Barwari K, de Bruin DM, Cauberg ECC, et al. Advanced diagnostics in renal mass using optical coherence tomography: a preliminary report. J Endourol. 2011; 25:311. [PubMed: 21235359]
19. Izatt JA, Hee MR, Owen GM, et al. Optical coherence microscopy in scattering media. Opt Lett. 1994; 19:590. [PubMed: 19844382]
20. Aguirre, AD. Thesis. Cambridge: Massachusetts Institute of Technology; 2008. Advances in Optical Coherence Tomography and Microscopy for Endoscopic Applications and Functional Neuroimaging.
21. Aguirre AD, Chen Y, Bryan B, et al. Cellular resolution ex vivo imaging of gastrointestinal tissues with optical coherence microscopy. J Biomed Opt. 2010; 15:016025. [PubMed: 20210470]
22. Delahunt B, Eble JN, McCredie MRE, et al. Morphologic typing of papillary renal cell carcinoma: comparison of growth kinetics and patient survival in 66 cases. Hum Pathol. 2001; 32:590. [PubMed: 11431713]
23. Morra MN, Das S. Renal oncocytoma: a review of histogenesis, histopathology, diagnosis and treatment. J Urol. 1993; 150:295. [PubMed: 8326547]
24. Remzi M, Javadli E, Ozsoy M. Management of small renal masses: a review. World J Urol. 2010; 28:275. [PubMed: 20177900]
25. Sofikerim M, Tatlisen A, Canoz O, et al. What is the role of percutaneous needle core biopsy in diagnosis of renal masses? Urology. 2010; 76:614. [PubMed: 20110106]

26. Aron M, Gill IS. Minimally invasive nephron-sparing surgery (MINSS) for renal tumours—part II: probe ablative therapy. Eur Urol. 2007; 51:348. [PubMed: 17084513]

Abbreviations and Acronyms

3D	3-dimensional
CC-RCC	clear cell RCC
CT	computerized tomography
OCM	optical coherence microscopy
OCT	optical coherence tomography
PN	partial nephrectomy
P-RCC	papillary RCC
RCC	renal cell carcinoma
RMB	renal mass biopsy
SRM	small renal mass

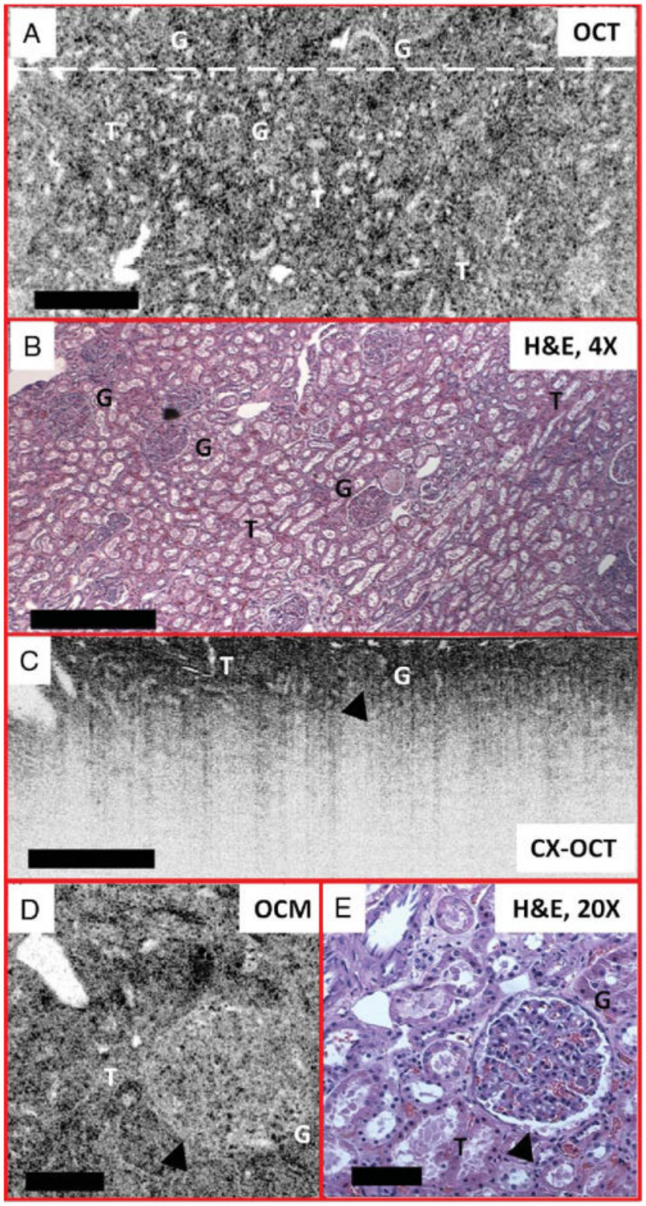

Figure 1.

Normal renal cortex. En face OCT image at depth of about 150 μm (*a*) and corresponding histological section (*b*) demonstrate architectural features of normal cortex, including glomeruli (*G*) and convoluted tubules (*T*). Cross-sectional OCT (*CX-OCT*) image (*c*) corresponds to scanning position marked as white dashed line in (*a*). OCM image acquired at depth of about 20 μm (*d*) and corresponding histological section (*e*) reveal glomerulus with surrounding convoluted tubules. Round pale regions represent complex network of glomerular capillaries (*d*). Scale bars represent 500 (*a* to *c*) and 100 (*d* to *e*) μm.

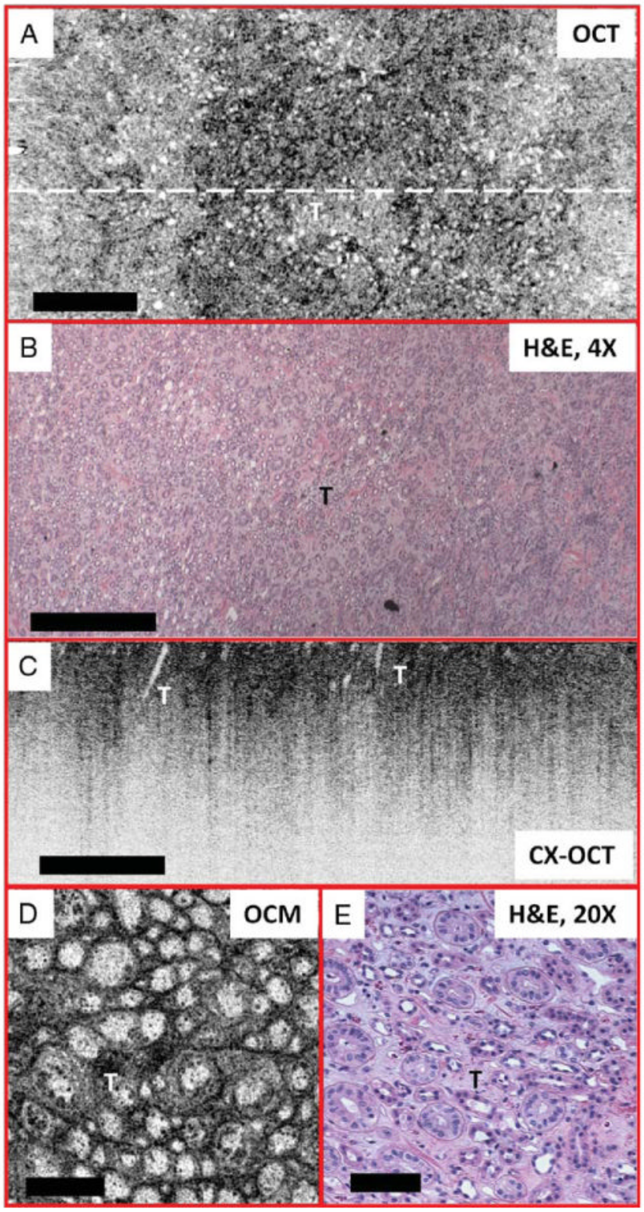

Figure 2.

Normal renal medulla. En face OCT image at depth of about 30 μm beneath tissue surface (*a*) and corresponding histological section (*b*). Cross-sectional OCT (*CX-OCT*) image, corresponding to scanning position marked as white dashed line in (*a*), reveals long straight tubules (*T*) elongating beneath tissue surface (*c*). OCM image about 30 μm beneath tissue surface (*d*) and corresponding histological section (*e*) show architectural features of medullary structures (*T*), corresponding to collecting tubules and loops of Henle. Scale bars represent 500 (*a* to *c*) and 100 (*d* to *e*) μm.

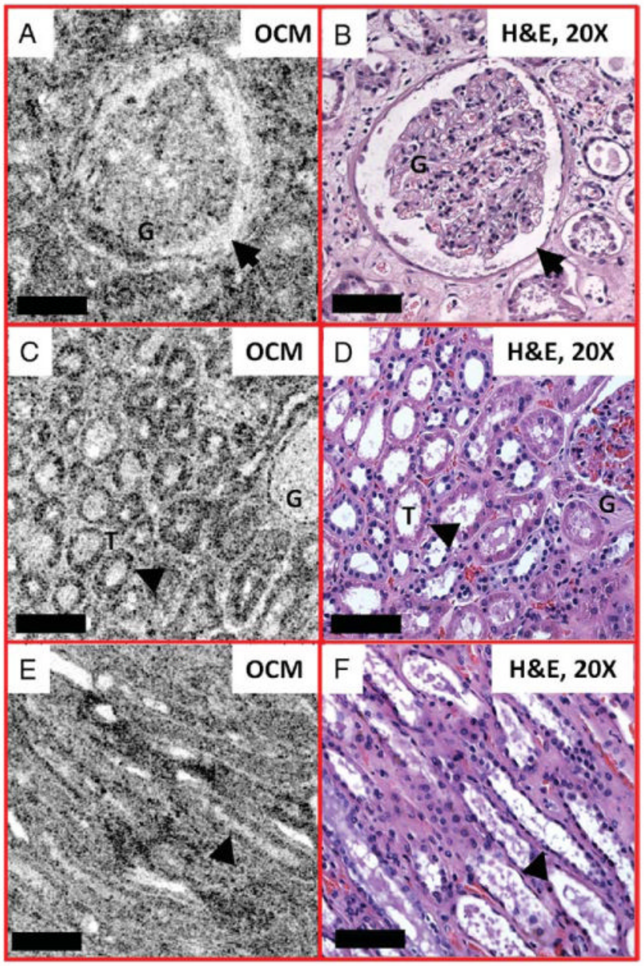

Figure 3.

OCM (*a*, *c* and *e*) and corresponding histological images (*b, d* and *f*) of normal kidney. Glomerulus (*G*) about 80 *μ*m beneath tissue surface (*a* and *b*). Arrows indicate Bowman's capsule (*a* and *b*). Convoluted tubules (*T*) (*c* and *d*), and collecting tubules and loops of Henle (arrowhead) of medulla (*e* and *f*). Higher magnification revealed these normal kidney functional units in more detail. Scale bars represent 100 *μ*m.

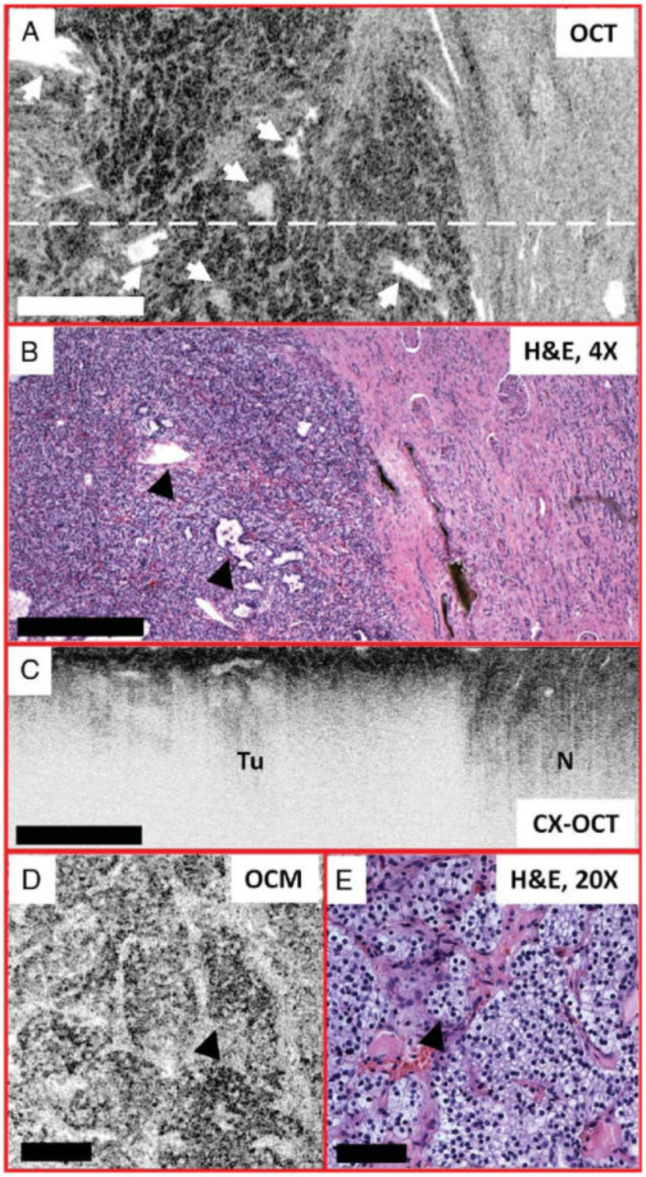

Figure 4.

CC-RCC. OCT image at depth of about 50 μm (*a*) of tumor interface with adjacent normal tissue and corresponding histological section (*b*). Arrows indicate hyposcattering features often seen in tumors (*a*). Cross-sectional OCT (*CX-OCT*) image at scanning position marked as white dashed line in (*a*) reveals differences in imaging depth between normal tissue (*N*) and tumor (*Tu*) (*c*). OCM image at depth of about 20 μm (*d*) and corresponding histological section (*e*). Arrowhead indicates tumor cells (*d* and *e*). Scale bars represent 500 (*a* to *c*) and 100 (*d* and *e*) μm.

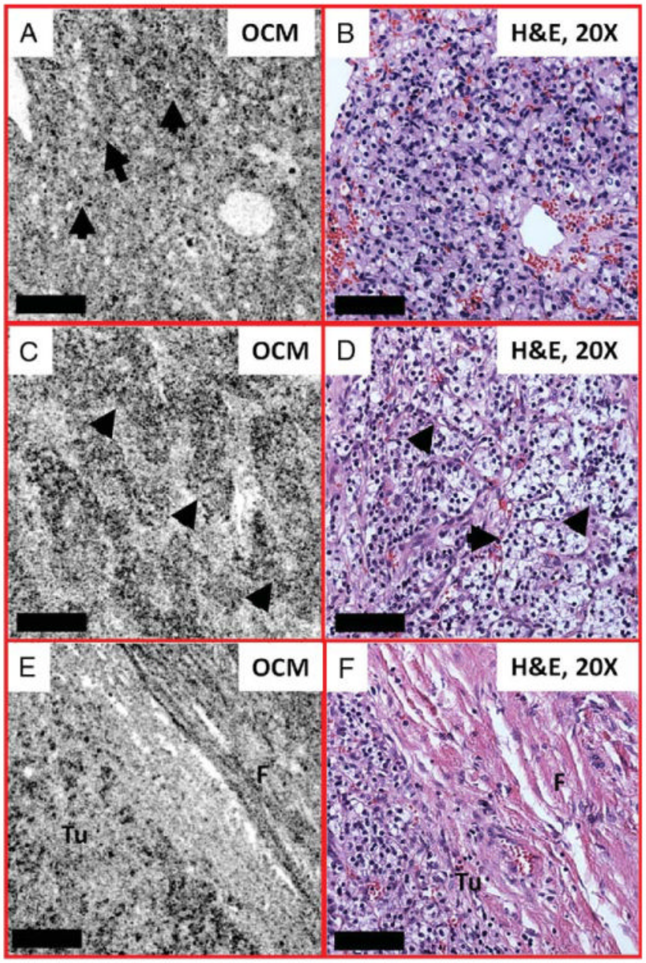

Figure 5.

OCM (*a*, *c* and *e*) and corresponding histological images (*b, d* and *f*) of CC-RCC. On OCM image about 30 μm beneath tissue surface tumor lacked fibrous septations over larger solid areas (*a*). Arrows indicate hyperscattering spots. On OCM image (*c*) about 15 μm beneath tissue surface over more typical region was noted with tumor cells arranged in nests (arrowheads) separated by delicate fibrous septae (*c* and *d*). Interface between tumor (*Tu*) and adjacent fibrous stroma (*F*) in normal kidney region (*e* and *f*). Scale bars represent 100 μm.

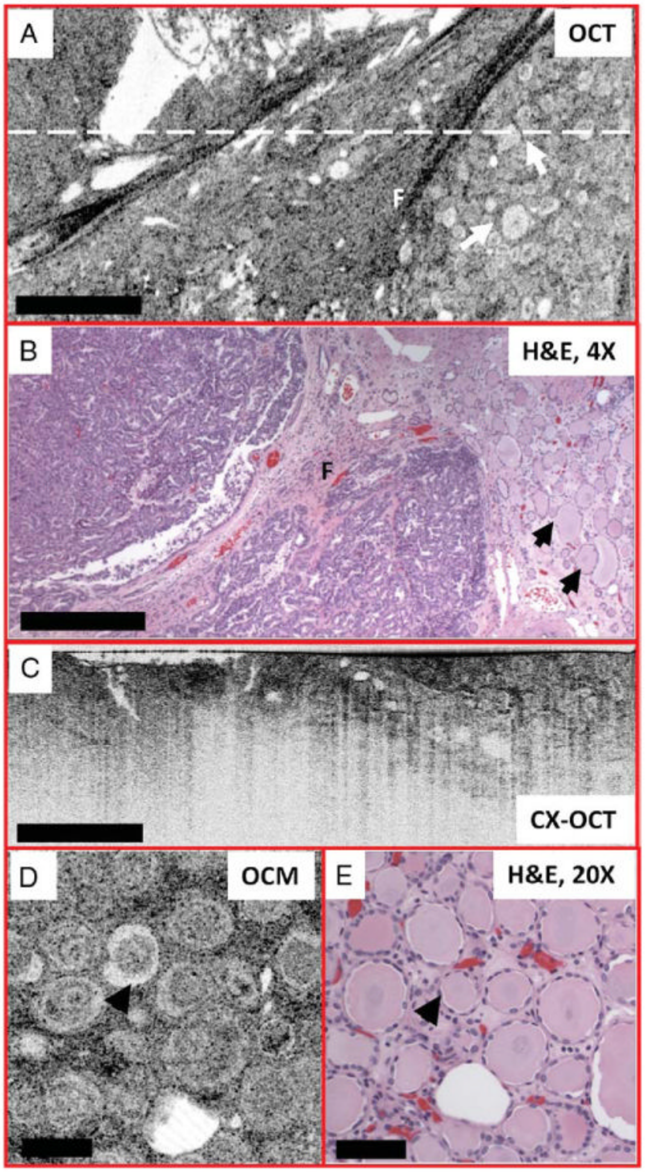

Figure 6.

P-RCC. En face OCT image at depth of about 50 μm (*a*) and corresponding histological section (*b*) of interface boundary between P-RCC and surrounding abnormal region. Kidney thyroidization was noted, shown as round follicle-like structures (arrows) (*a* and *b*). *F*, fibrous stroma. Cross-sectional OCT (*CX-OCT*) image at scanning position marked as white dashed line in (*a*) (*c*). OCM image at depth of about 15 μm (*d*) and corresponding histological section (*e*) more clearly reveal hyposcattering structures (arrowhead) reminiscent of thyroid follicles. Scale bars represent 500 (*a* to *c*) and 100 (*d* to *e*) μm.

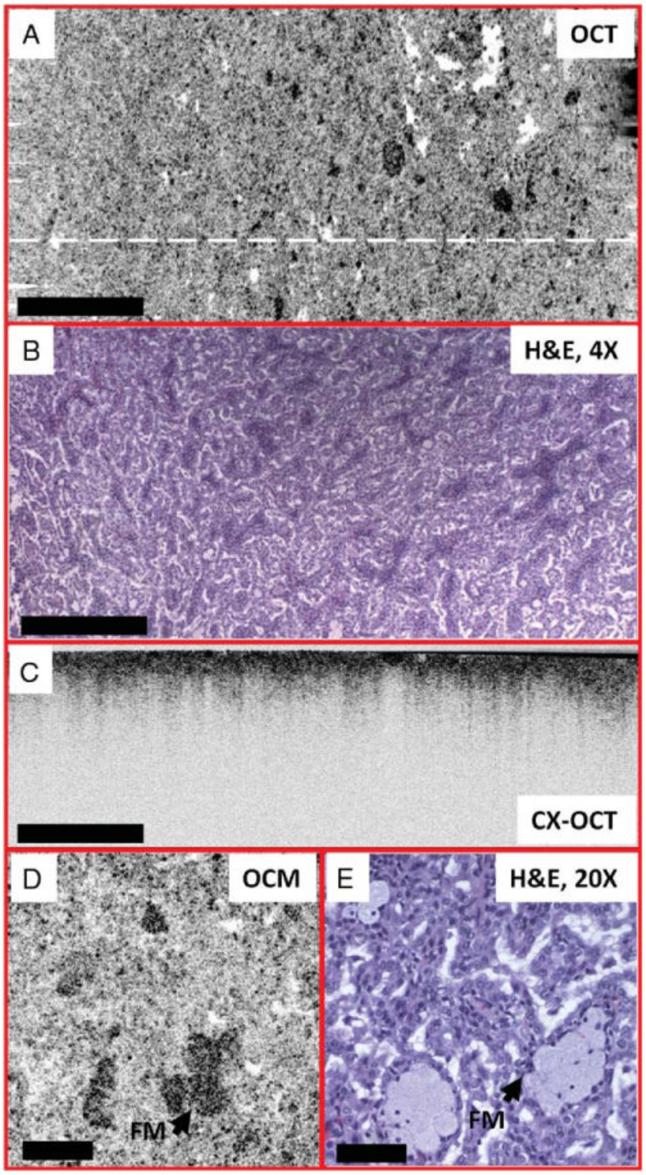

Figure 7.

P-RCC. En face OCT image at depth of about 50 μm (*a*) and corresponding histological section (*b*) in tumor. Cross-sectional OCT (*CX-OCT*) image at scanning position marked as white dashed line in (*a*) shows limited imaging depth due to tumor cell overgrowth (*c*). OCM image at depth of about 15 μm (*d*) and corresponding histological section (*e*) reveals tumor containing foamy macrophages (*FM*). Scale bars represent 500 (*a* to *c*) and 100 (*d* to *e*) μm.

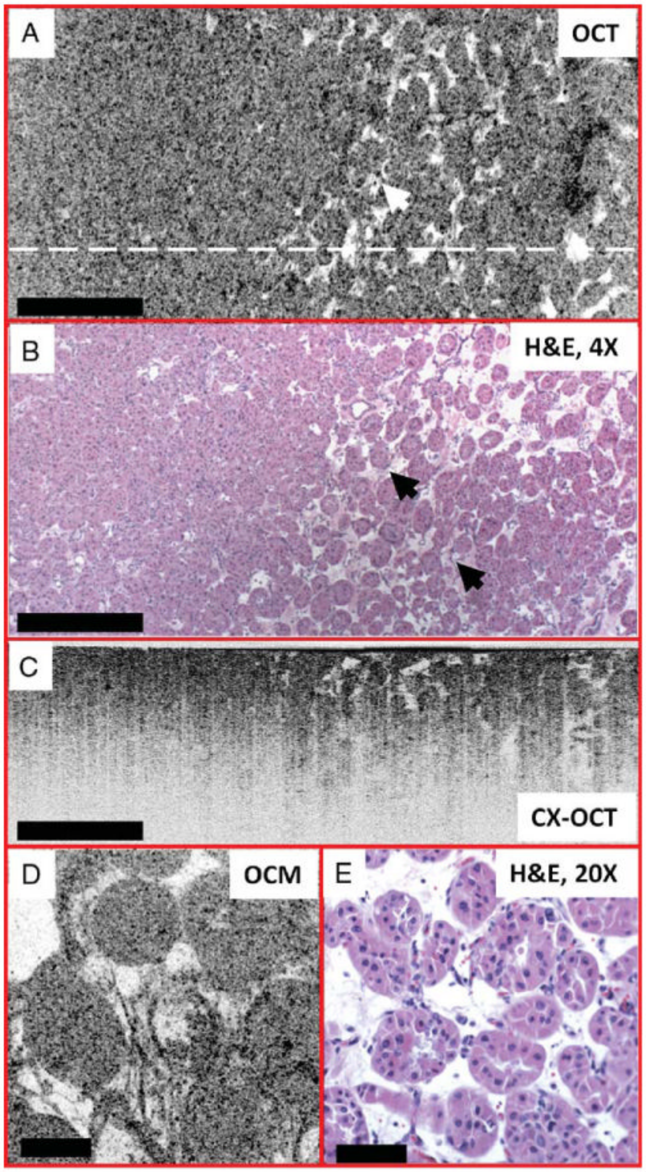

Figure 8.

Oncocytoma. En face OCT image at depth of about 60 μm (*a*) and corresponding histological section (*b*) reveals oncocytoma nested growth pattern (arrows). Cross-sectional OCT (*CX-OCT*) image at scanning position marked as white dashed line in (*a*) shows morphology along depth dimension (*c*). OCM image at depth of about 30 μm (*d*) and corresponding histological section (*e*) demonstrate oncocytoma nested growth pattern. Scale bars represent 500 (*a* to *c*) and 100 (*d* to *e*) μm.